

# Incoherent Diffraction Imaging with a Pseudo-Thermal Light Source

PABLO SAN MIGUEL CLAVERIA,<sup>1,\*</sup> SEBASTIÃO ANTUNES<sup>1</sup>, PEER BIESTERFELD<sup>2</sup>, MATILDE FERNANDES<sup>1</sup>, MATILDE GARCIA<sup>1</sup>, MATILDE NUNES<sup>1</sup>, LUCAS ANSIA FERNANDEZ<sup>1</sup>, GARETH O. WILLIAMS<sup>1</sup>, SVEN FROEHLICH<sup>2</sup>, DAVID THEIDEL<sup>3</sup>, PHILIP MOSEL<sup>2</sup>, IHSAN FSAIFES<sup>4</sup>, ANDREA TRABATTONI<sup>2,5</sup>, MARCO PICCARDO<sup>6,7</sup>, JEAN-CHRISTOPHE CHANTELOUP<sup>4</sup>, MILUTIN KOVACEV<sup>2</sup>, HAMED MERDJI<sup>3</sup>, AND MARTA FAJARDO<sup>1</sup>

<sup>1</sup>GoLP/Instituto de Plasmas e Fusão Nuclear, Instituto Superior Técnico, Universidade de Lisboa, Lisbon, 1049-001, Portugal.

<sup>2</sup>Institut für Quantenoptik, Leibniz Universität Hannover, Hannover 30167, Germany

<sup>3</sup>Laboratoire d'Optique Appliquée, ENSTA Paris, CNRS, Ecole Polytechnique, Institut Polytechnique de Paris, Palaiseau, France

<sup>4</sup>LULI, CNRS, Ecole Polytechnique, CEA, Sorbonne Université, Institut Polytechnique de Paris, 91120 Palaiseau, France

<sup>5</sup>Center for Free-Electron Laser Science CFEL, Deutsches Elektronen-Synchrotron DESY, Hamburg, Germany

<sup>6</sup>Department of Physics, Instituto Superior Técnico, Universidade de Lisboa, Lisbon, Portugal

<sup>7</sup>Instituto de Engenharia de Sistemas e Computadores – Microsistemas e Nanotecnologias (INESC MN), Lisbon, Portugal

\*[pablo.san.miguel.claveria@tecnico.ulisboa.pt](mailto:pablo.san.miguel.claveria@tecnico.ulisboa.pt)

## Abstract:

Incoherent Diffraction Imaging - IDI - is a diffraction-based imaging technique that has been recently proposed to exploit the partial coherence of incoherently scattered light to retrieve structural information from the scattering centers. Similar to the stellar intensity interferometry of Hanbury Brown and Twiss, the signal builds up on the second-order spatial correlations of the emitted light. The complex spatial distribution of the target is thereby encoded in the spatial intensity fluctuations of the scattered light. The first experimental realisations of this imaging technique have been realised using the fluorescence excited by an ultra-short X-ray pulse at Free Electron Laser (FEL) facilities. Here, we propose an alternative set-up based on a table-top Pseudo-Thermal Light Source. This set-up allows us to explore IDI under a wide range of physically relevant conditions as well as to benchmark numerical and analytical models currently used to determine the imaging capabilities of this technique.

## 1. Introduction

The coherence of light, or the spatial and temporal phase carried by a light source, has been decisive for imaging at short wavelengths, where diffraction-limited optics are unavailable. Coherent diffraction imaging (CDI), which makes use of the diffraction pattern of coherent light from an object to retrieve the real space image of the object, relies on sources with high degree of spatial and temporal coherence, reaching spatial resolutions limited only by the wavelength. After its first experimental demonstration [1], CDI has successfully validated single shot femtosecond nanoscale imaging [2, 3] with the possibility to extend to 3D perception [4–6]. Especially, illumination with short wavelengths like X-Rays for imaging of biological samples has been widely adopted [7, 8]. However, its range of applicability is currently limited by the small number of light sources that can produce bright X-rays with the required degree of temporal and spatial coherence. Indeed, the most relevant implementation of CDI techniques are often carried out in

one of the few Free Electron Laser (FEL) facilities around the globe.

Recently, a new diffraction-based imaging technique has been proposed [9] to exploit second-order (intensity) correlations of partially coherent light. In analogy to CDI, it was named Incoherent Diffraction Imaging (IDI), highlighting its reliance on a comparatively lower degree of coherence. This technique requires the recording of the diffracted light within a timescale shorter or comparable to the coherence time,  $\tau_c$ , of the light field. Hence the recorded diffraction pattern can be considered stationary during the acquisition time, as naturally happens in CDI. Whereas the diffraction pattern will fluctuate for each individual acquisition, the autocorrelation of the recorded intensity is insensitive to these spatial variations and will thus progressively build-up when averaging over multiple acquisitions. Being based on intensity correlations, this technique shares the working principle with the intensity interferometer originally proposed by Hanbury Brown and Twiss to overcome atmospheric distortions on the light coming from the stars. However, instead of using two spatially separated Photo-Multiplier Tubes, the spatial correlation is carried out on the intensity of the light measured by a pixelized detector.

One of the most promising applications of IDI is to retrieve the structural information of an object via incoherent scattering processes, namely fluorescence [10]. Fluorescence is typically considered as incoherent light due to the quantum (random) nature of its emission, with a coherence time given by the radiative lifetime of the corresponding transition, i.e. inversely proportional to the spectral linewidth  $\Gamma$  ( $\tau_c = 2\hbar/\Gamma$ ) [11]. For inner-shell fluorescence of transition metal atoms - one of the most narrow linewidth emissions- one finds that  $\tau_c$  is of the order of fs (0.82 fs for Fe, 0.62 fs for Cu). Most advanced FELs facilities are currently able to produce X-ray pulses with pulse durations of the order of these timescales, and thus the fluorescence excited by these FEL pulses can be temporally gated for durations of the order of its coherence time. Therefore, in a single shot, a good degree of temporal coherence can be obtained from inner-shell fluorescence in solids excited by a fs FEL pulse. However, each shot will produce a different relative phase between positions on the emitted wavefront, causing variations in the pattern on the detector from shot to shot. Contrary to CDI, the accumulation of multiple patterns on the detector does not result in an improved signal to noise ratio, rather a loss of information as the stochastic spatial variations in each shot lead to blurring of any diffracted signals when accumulated.

In order to increase the visibility of the measured spatial pattern, IDI relies on accumulating the second-order spatial correlations of the light field, i.e. the spatial auto-correlations of the recorded intensity, which is insensitive to the phase variations between each fluorescence event [12]. In this way, the structural information of the emitters of incoherently scattered light can be retrieved from the second order correlation by recalling the Siegert relation [13] for a Thermal Light Source (TLS)<sup>1</sup>, that relates the first and second order correlations as

$$g^{(2)}(\vec{q}) = 1 + \beta |g^{(1)}(\vec{q})|^2 \quad (1)$$

where  $g^{(2)}(\vec{q})$  is the normalised intensity auto-correlation and  $g^{(1)}(\vec{q})$  is the normalised scattering amplitude (the strength of the coherent diffraction pattern at a particular object's spatial frequency  $\vec{q}$ ). The visibility parameter  $\beta$  accounts for the partial temporal coherence of the recorded light ( $0 < \beta \leq 1$ ). For a fully coherent illumination, the visibility  $\beta = 1$ .

Other works have used intensity correlations from inner-shell fluorescence of Cu atoms excited by a short FEL pulse to determine the focal spot size [14] and pulse duration [15] of the incoming X-ray pulse. Moreover, the first imaging experiment of a non-trivial structure using IDI [16] was carried out at the MID instrument of the European XFEL [17]. By focusing the FEL pulse onto two spatially separated focal spots on a thin Cu target, the associated second-order spatial fringes were observed in the intensity correlation map after accumulating  $5.8 \times 10^7$  fluorescence

---

<sup>1</sup>Valid in the limit of a large number of emitters [12]

frames. From this  $g^{(2)}(\vec{q})$  map, the size and separation of the two X-ray spots was correctly reconstructed.

The large number of frames and the associated long acquisition time ( $\approx 5$ h) are a consequence of the low number of averaged detected photons per pixel per frame  $\mu = 7.7 \times 10^{-3}$  and the rather long FEL pulse duration (6.2 fs, compared to the Cu fluorescence  $\tau_c \approx 0.6$  fs), which in this experiment ultimately resulted in  $\beta = 0.018$ . According to analytical and numerical models [12], these long acquisition times can be greatly reduced with shorter excitation pulses (3 minutes for 3 fs pulses) and with brighter fluorescence sources. These long acquisition times, coupled with the high demand for XFEL access, means that imaging of more complex objects has been so far elusive. Furthermore, rigorous tests of the imaging performance of IDI for physically relevant parameters, such as coherence time and source brightness, are needed to fully understand the imaging capabilities of this new technique. In this letter, we demonstrate a table-top experimental set-up based on a Pseudo-Thermal Light Source to experimentally explore IDI and benchmark analytical and numerical models. Although Pseudo-Thermal Light Sources have been explored for diffraction-based imaging [18–20], here we extend the use of the PTLs to experimentally study the effect of the second-order temporal coherence on the visibility  $\beta$  of the retrieved  $g^{(2)}$ , which can then be extrapolated to the short-wavelength regime where diffraction-based imaging techniques are of most use. The first section describes the proposed optical set-up, including a thorough characterisation of the degree of coherence of the PTLs. The second section shows acquisitions that evidence the performance of IDI in retrieving structural information from the emitters. Finally, we provide quantitative measurements of the imaging performance of our IDI set-up over a wide range of physical parameters, comparing these measurements with existing analytical and numerical models. In this way, we aim to provide a new experimental approach, as well as experimental evidence of the feasibility of the method.

## 2. Experimental set-up

In order to build a Pseudo-Thermal Light Source with a large degree of tunability in terms of coherence, we have used a ground-glass diffuser with 1500 grit/mm mounted on a motorised rotation stage, which is illuminated by a CW diode laser of  $\lambda = 660$  nm. On the one hand, such a PTLs allows to control the spatial coherence of the diffused light, i.e. the speckle size, via the illumination area (laser spot size) on the diffuser and the distance between the diffuser and the spatially resolved detector [13]. On the other hand, for a given illumination area, the second-order temporal coherence can be controlled by the rotation speed of the diffuser. Note that the second-order temporal coherence is also inversely proportional to the illumination area [21, 22], and thus for the same diffuser rotation speed different illumination areas lead to different degrees of second-order temporal coherence. Ultimately, the brightness of this PTLs, namely the number of photons per pixel per frame  $\mu$  can be controlled via the laser power and additional filtering.

The diffused light is recorded with a CMOS camera placed at  $\approx 18$  cm away from the diffuser with a small lateral offset with respect to the optical axis to avoid the specular part of the laser beam that is not scattered. The distance from the pixelised detector to the diffuser was chosen to ensure enough speckle sampling [23]. In this experiment the temporal gating of the incoherent light is carried out via the exposure time of the detector (i.e. we gate the light detection instead of the light emission), which allows us to control the degree of visibility  $\beta$  in our IDI acquisitions. In addition, we use a Spatial Light Modulator (SLM) together with a Fourier lens to holographically control the intensity distribution [24] impinging on the diffuser and thus create any arbitrary test object. The SLM-generated intensity distribution that is sent to the diffuser is recorded with an additional camera by picking part of the incoming beam with a beam splitter. A schematic of the experimental set-up is shown in Fig. 1(a). This flexible optical set-up allows the retrieval of structural information of the SLM-generated intensity distribution by computing the second-order

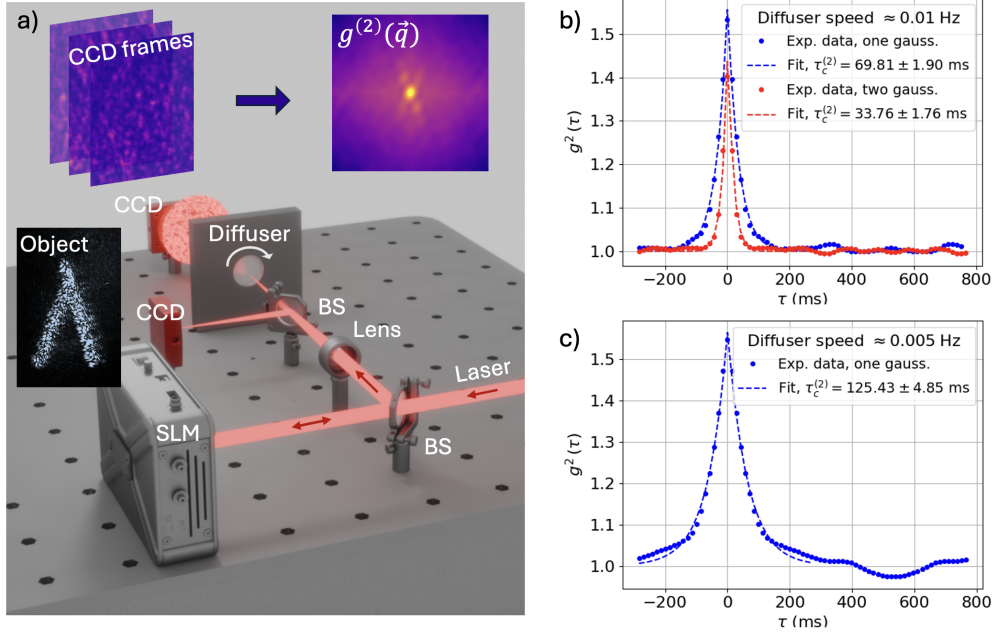


Fig. 1. (a) Sketch of experimental set-up. The laser comes from the right of the image, goes through the beam splitter (BS), reflects at the SLM chip (where it acquires the holographic phase corresponding to desired object intensity), reflects from the same BS towards a plano-convex lens and is then focused on the rotating diffuser. An additional BS is placed between the lens and the diffuser to monitor the laser intensity at the focal plane of the lens. Two CMOS cameras are used to record the aforementioned laser intensity at the focal plane of the lens as well as the diffused light. The inset show examples of object intensities, three frames of recorded diffused light, and the  $g^{(2)}$  auto-correlation map computed from 100 frames. (b)  $g^{(2)}(\vec{q} = 0, \tau)$  experimental measurements for a single and double Gaussian intensity distributions impinging onto the diffuser, and associated Lorentzian fits from which the  $\tau_c^{(2)}$  is extracted (see legend). (c) Same as (b) but for a diffuser rotating at twice the speed of (b).

correlations of the diffused light recorded by the detector.

In contrast to other imaging experiments based on high-order correlations from a Pseudo-Thermal Light Source [19], in this set-up the diffuser acts both as a source of pseudo-thermal light and as the object to be reconstructed, mimicking the fluorescence-based IDI experiments. Whereas the use of an SLM to control the intensity distribution sent to the diffuser poses some limitations in terms of minimum object size and resolution, it offers a large degree of versatility to explore different object complexities without the need of machining new object masks. Examples of object distributions created using this set-up are shown in Fig. 2.

In order to assess the second-order temporal coherence of the source, we measured the second order temporal correlation function

$$g^{(2)}(\tau) = \frac{\langle I(t)I(t+\tau) \rangle}{\langle I(t) \rangle^2} \quad (2)$$

where the average is performed over time  $t$  and over  $100 \times 100$  pixels of the detector. Fig. 1(b) and (c) show the results of these measurements for two rotation speeds 0.01 Hz and 0.005 Hz (blue dots) when a Gaussian intensity pattern impinges the diffuser, as well as the fitted Lorentzian curves whose associated second-order temporal coherence  $\tau_c^{(2)}$  is shown in the legend. For these

acquisitions, taken with a detector exposure time of 5 ms, we measure a second-order temporal coherence ranging from 10s to 100s of ms. As expected, the retrieved  $\tau_c^{(2)}$  is proportional to the rotation speed of the diffuser. Moreover, Fig. 1(b) also shows the measured second order temporal coherence when two spatially separated Gaussian distributions of the same size as the single Gaussian pattern impinge on the diffuser (red dots). As expected, the retrieved  $\tau_c^{(2)}$  is reduced by a factor of two due to the doubled area of the diffuser that is illuminated [21].

### 3. Measuring $g^{(2)}$ with a PTLs

We now show how second order spatial correlations can be used to extract structural information of the scatterers distribution given the finite degree of coherence of a PTLs. For these acquisitions, shown in Fig. 2, we set the coherence time of the PTLs ( $\sim 100$  ms) to be significantly longer than the exposure time of the detector (5 ms) in order to detect a single temporal mode. In this Fig. 2, each row corresponds to a different object intensity distribution, which are shown on the first column Fig. 2(a,b,c).

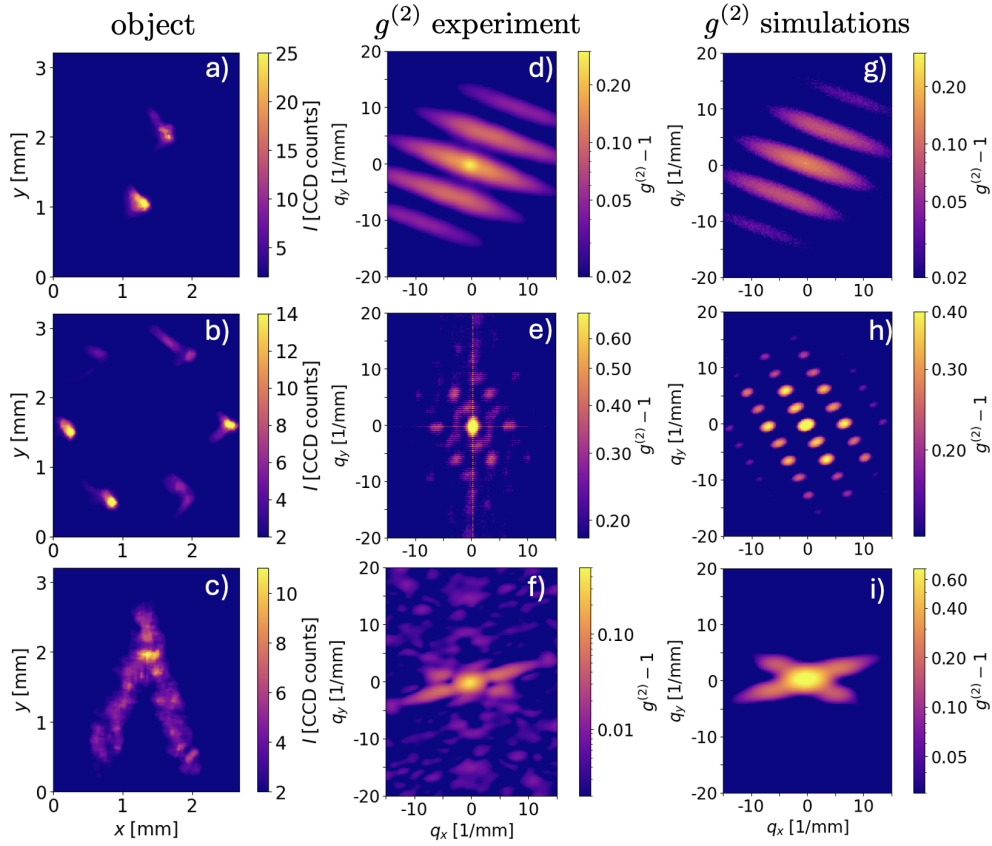


Fig. 2. Three exemplary IDI acquisitions performed with our PTLs-based set-up. Sub-figures (a,d,g) show the recorded intensity distribution impinging the rotating diffuser. Sub-figures (b,e,h) show the computed  $g^{(2)} - 1$  from 100 acquisitions of the diffused light. Sub-figures (c,f,i) show the associated computed  $g^{(2)} - 1$  from 100 simulated frames. See text for further details.

After computing and averaging the intensity auto-correlations over 100 frames using  $400 \times 400$  pixels, the normalised  $g^{(2)}(\vec{q})$  maps are shown on Fig. 2(d,e,f). Note that for the calculation

of the intensity auto-correlations we roll each frame on itself in order to have a same number of realisations for each  $q$  [12]. The diffraction patterns associated to each object intensity distribution are clearly visible in these second order spatial correlations, despite the varying level of visibility. It should be noted that for these acquisitions the number of frames (100) is enough to reach the maximum visibility given the large number of photons per pixel per frame  $\mu \gtrsim 1$ .

We have also performed numerical simulations to assess the level of visibility of the measured second order correlation maps. Similarly to [12], these simulations use Fresnel propagation to propagate the object intensity distribution measure in the experiments with a randomised phase from the diffuser to the detector plane. In order to account for the degree of temporal coherence, we add the propagated intensity over several randomisations of the initial phase. In this way we can simulate the detection of an integer number of temporal modes  $N_{rmM}$  when the detector detection time is greater than  $\tau_c$ . Moreover, we include the Poisson statistics associated to the CMOS detector photon detection to generate synthetic frames. This simulation tool is accessible in [25] for researchers to quickly check the feasibility of their imaging conditions.

The  $g^{(2)}(\vec{q})$  computed from 100 synthetic frames generated by the corresponding intensity distributions showed in Fig. 2(a,b,c) with a single temporal mode are displayed on Fig. 2(g,h,i). Overall these simulated  $g^{(2)}(\vec{q})$  maps reproduce well the experimental features. The main source of discrepancy between the experiment and simulations originates from the higher levels of background in the  $g^{(2)}(\vec{q})$  maps computed from experimental data, likely due to thermal variations in the Poisson statistics of the CMOS detector electronics. This higher background levels result in the loss of some features of the  $g^{(2)}(\vec{q})$ , specially as the object structure becomes more complex. Recalling the Siegert relation (Eq. 1), the real-space distribution of the object intensity can be recovered using existing phase retrieval algorithms [16], or recently developed adaptations for higher-order light correlations [26, 27].

The object intensity distributions shown in Fig. 2(a,b) were mostly intended to reproduce, respectively, what was done in the first IDI experiment [16] and the first high-order correlation imaging experiment [19], which is restricted to retrieve the finite number of spatial frequencies of a discrete object distribution. The example shown in Fig. 2(c) is, to our knowledge, the first implementation of IDI on a continuous isolated object, a letter  $\lambda$  in this case.

#### 4. Assessing imaging capabilities of IDI

The versatility of this PTLS optical set-up in terms of brightness and degree of coherence can be exploited to benchmark the analytical and numerical models of IDI that have been developed over the recent years [12, 28]. Of special importance are the scalings of the visibility for different source brightness (in terms of average number of photons per shot per pixel  $\mu$ ) and number of temporal modes accumulated in each frame. For a PTLS, this can be defined as [13]

$$\mathcal{M} = \left[ \frac{1}{T} \int_{-T}^T \left( 1 - \left| \frac{\tau}{T} \right| \right) |\gamma(\tau)|^2 d\tau \right]^{-1} \quad (3)$$

where  $T$  is the camera acquisition time and  $\gamma(\tau)$  is the complex degree of coherence, for which we use the fitted function shown in Fig. 1(b). Note that, when  $T \gg \tau_c$ , we can approximate  $\mathcal{M} \approx \frac{T}{\tau_c}$ , i.e. the ratio between the duration of the acquisition of each frame and the temporal coherence of the light source. For simplicity, we are going to restrict our study to the object intensity distribution used for the first experimental realisation of IDI in an FEL facility [16], two spatially separated illumination areas as shown in Fig. 2(a).

In Fig. 3(a) we plot the outlines of the  $g^{(2)} - 1$  maps (perpendicular to the fringes) for different number of temporal modes  $\mathcal{M}$  accumulated in each acquisition. Experimentally, the number of temporal modes is controlled via the diffuser rotation speed. Other parameters such as detector exposure time (1 ms), average number of photons per pixel per frame  $\mu \approx 0.1$  and total number of frames (100) are kept constant. As expected, the contrast of the fringes decreases as  $\mathcal{M}$  increases.

Since the signal cannot be readily separated from background and noise, we have followed a similar approach as in [12] to quantify the level of visibility and noise under different experimental conditions. We have fitted these outlines to the ground truth fringe pattern [29] multiplied by an amplitude ( $S$ ) plus a constant background ( $B$ ), i.e.  $G^{(2)} = B + S|g^{(1)}(q)|^2$ , with  $S$  and  $B$  as free parameters. We define the Signal-to-Background ratio (SBR) as the ratio between  $S$  and  $B$ , and the Signal-to-Noise ratio (SNR) as the Signal divided by the standard deviation of the error, i.e. the difference between the best-fit and the experimental data. We have computed these SBR and SNR for different average number of photons per pixel per frame  $\mu$  and different number of accumulated temporal modes. The results are shown in Fig. 3 (b) and (d). Using 100 frames for the calculation of each  $g^{(2)}(\vec{q})$ , we found an optimal SBR of  $\approx 0.7$  for a large enough brightness ( $\mu \gtrsim 0.1$ ) and for  $\mathcal{M} \sim 1$ . For the same number of total frames, either increasing the detected number of temporal modes or decreasing the source brightness leads to a decrease of visibility.

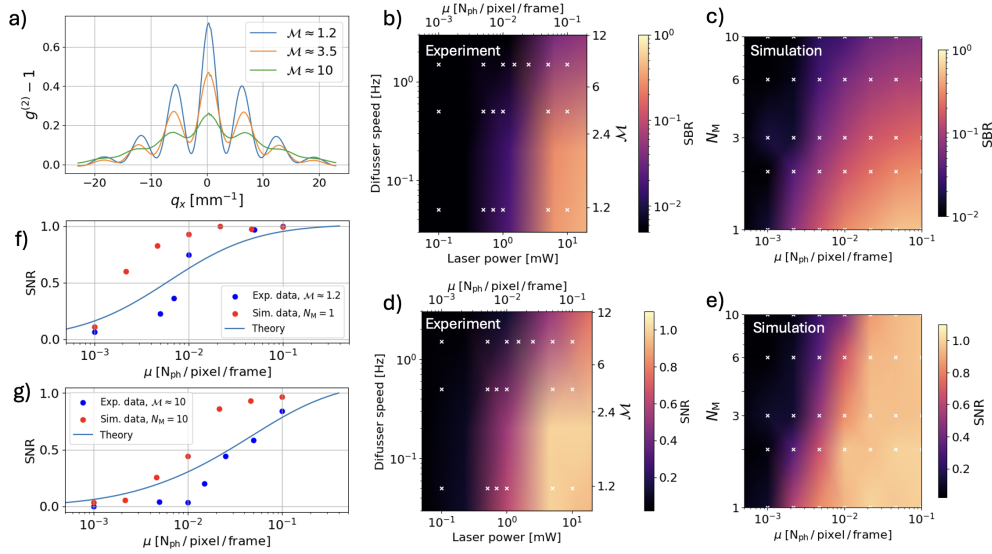


Fig. 3. (a) Second order fringes produced by a double Gaussian impinging onto the ground-glass diffuser for different degrees of temporal coherence, i.e. accumulated temporal modes. (b) Measured SBR (see text for details) for different  $\mu$  and  $\mathcal{M}$  ( $N_M$ ). The actual measurements were performed at the white crosses, and the colormap shows interpolated results. (c) Equivalent SBR extracted from simulations. (d) Measured SNR. (e) Equivalent SNR extracted from simulations. (f) SNR as a function of  $\mu$  for  $\mathcal{M} \approx 1$  as measured from experimental data (blue dots), as extracted from simulations (red dots), and given by analytical model (blue line). (g) Same as (f) but for  $\mathcal{M} \approx 10$ .

Furthermore, we have used the previously explained simulation framework to compare the experimental measurements of SBR and SNR with numerical simulations performed with the same range of physical parameters. The results of these simulations are shown in Fig. 3 (c) and (e). Note that in these simulations only an integer number of temporal modes  $N_M$  can be simulated. Overall, a good agreement is found between these simulations and the experimental measurements. A similar value for the optimal visibility of  $\approx 0.7$  is observed in these simulations at the same optimal conditions within our parameter range, as well as similar trends are also retrieved. Horizontal outlines of these colormaps for  $\mathcal{M} \sim 1$  and  $\mathcal{M} \sim 10$ , with both experimental and simulation results, are also shown in Fig. 3 (f) and (g). In order to compare these trends to existing analytical models, these plots also include the theoretical scaling of the SNR for a crystalline

structure [12]:

$$\text{SNR}_{\text{Crystal}} \propto \frac{\mu^2}{\mathcal{M} \sqrt{\frac{1+4\mathcal{M}}{\mathcal{M}^2} \mu^4 + 2 \frac{1+2\mathcal{M}}{\mathcal{M}} \mu^3 + \mu^2}} \quad (4)$$

The overall trends observed both in simulations and experimental data are in good agreement with this scaling, both with respect to  $\mu$  and  $\mathcal{M}$ . It should be noted that a similar discrepancy between this scaling and simulation of non-crystalline objects was observed in the aforementioned theoretical study, and was associated to the strong dependence of the SNR on the object complexity.

## 5. Conclusions

In this article, we have presented an original table-top optical set-up that allows to validate of Incoherent Diffraction Imaging approach using a Pseudo-Thermal Light Source. This set-up has enabled us to experimentally explore IDI over an unprecedented range of physically relevant parameters such as the degree of coherence of the scattered light and the brightness of the light source. Whereas the first experimental realisations of IDI were carried out at FEL facilities, at the wavelength range (X-rays) where this technique holds the promise to unlock high resolution diffraction-based imaging with partially coherent light sources, the restricted access to these facilities limits the amount of relevant experimental data that can be currently produced at this first testing stage of IDI. To address this challenge, we constructed a scaled experiment using a visible laser, rotating ground glass and spatial light modulator to simulate x-ray incoherent diffraction. This provides an accessible and versatile mean of studying the IDI technique before transitioning to large-scale X-ray facilities. This table-top set-up allows us to further explore the key parameters of the IDI approach at scale, offering experimental evidence of the scalings of the Signal-to-Background Ratio and Signal-to-Noise Ratio for different physically relevant conditions, namely low number of photons per pixel per frame, and large number of temporal modes ( $\sim 10$ ) detected at each acquisition. The measured visibility and trends are found to be in reasonably good agreement with existing numerical and analytical methods used to model IDI experiments. This set-up can experimentally benchmark the IDI methodology and thus efficiently address the potential of IDI to realize nanometer scale diffraction-based imaging using partially coherent light sources, without the need of performing fluorescence based experiments.

**Funding.** NanoXCAN is an European Council Pathfinder Project 101047223

**Acknowledgments.** The authors would like to thank Prof. Joachim von Zanthier for useful discussions, as well as to the anonymous reviewers for their valuable input to this manuscript.

**Disclosures.** The authors declare no conflicts of interest.

**Data availability.** Data underlying the results presented in this paper are available in Ref. [25].

## References

1. J. Miao, P. Charalambous, J. Kirz, and D. Sayre, "Extending the methodology of x-ray crystallography to allow imaging of micrometre-sized non-crystalline specimens," *Nature* **400**, 342–344 (1999).
2. H. N. Chapman, A. Barty, M. J. Bogan, *et al.*, "Femtosecond diffractive imaging with a soft-x-ray free-electron laser," *Nat. Phys.* **2**, 839–843 (2006).
3. A. Ravasio, D. Gauthier, F. R. N. C. Maia, *et al.*, "Single-shot diffractive imaging with a table-top femtosecond soft x-ray laser-harmonics source," *Phys. Rev. Lett.* **103**, 028104 (2009).
4. R. Neutze, R. Wouts, D. van der Spoel, *et al.*, "Potential for biomolecular imaging with femtosecond x-ray pulses," *Nature* **406**, 752–757 (2000).
5. I. K. Robinson, I. A. Vartanyants, G. J. Williams, *et al.*, "Reconstruction of the shapes of gold nanocrystals using coherent x-ray diffraction," *Phys. Rev. Lett.* **87**, 195505 (2001).
6. J. Duarte, R. Cassin, J. Huijts, *et al.*, "Computed stereo lensless x-ray imaging," *Nat. Photonics* **13**, 449–453 (2019).
7. A. Munke, J. Andreasson, A. Aquila, *et al.*, "Coherent diffraction of single rice dwarf virus particles using hard x-rays at the linac coherent light source," *Sci. Data* **3**, 160064 (2016).



8. Y. Nishino, Y. Takahashi, N. Imamoto, *et al.*, “Three-dimensional visualization of a human chromosome using coherent x-ray diffraction,” *Phys. Rev. Lett.* **102**, 018101 (2009).
9. A. Classen, K. Ayyer, H. N. Chapman, *et al.*, “Incoherent diffractive imaging via intensity correlations of hard x rays,” *Phys. Rev. Lett.* **119**, 053401 (2017).
10. P. J. Ho, C. Knight, and L. Young, “Fluorescence intensity correlation imaging with high spatial resolution and elemental contrast using intense x-ray pulses,” *Struct. Dyn.* **8**, 044101 (2021).
11. H. E. White *et al.*, *Introduction to Atomic Spectra* (McGraw-Hill Book Co., Inc., 1934).
12. F. Trost, K. Ayyer, and H. N. Chapman, “Photon statistics and signal to noise ratio for incoherent diffraction imaging,” *New J. Phys.* **22**, 083070 (2020).
13. J. W. Goodman, *Statistical Optics* (Wiley, 1985).
14. N. Nakamura, S. Matsuyama, T. Inoue, *et al.*, “Focus characterization of an X-ray free-electron laser by intensity correlation measurement of X-ray fluorescence,” *J. Synchrotron Radiat.* **27**, 1366–1371 (2020).
15. I. Inoue, K. Tamasaku, T. Osaka, *et al.*, “Determination of X-ray pulse duration via intensity correlation measurements of X-ray fluorescence,” *J. Synchrotron Radiat.* **26**, 2050–2054 (2019).
16. F. Trost, K. Ayyer, M. Prasciolu, *et al.*, “Imaging via correlation of x-ray fluorescence photons,” *Phys. Rev. Lett.* **130**, 173201 (2023).
17. A. Madsen, J. Hallmann, G. Ansaldi, *et al.*, “Materials Imaging and Dynamics (MID) instrument at the European X-ray Free-Electron Laser Facility,” *J. Synchrotron Radiat.* **28**, 637–649 (2021).
18. O. Katz, P. Heidmann, M. Fink, and S. Gigan, “Non-invasive single-shot imaging through scattering layers and around corners via speckle correlations,” *Nat. Photonics* **8**, 784–790 (2014).
19. R. Schneider, T. Mehringer, G. Mercurio, *et al.*, “Quantum imaging with incoherently scattered light from a free-electron laser,” *Nat. Phys.* **14**, 126–129 (2018).
20. T. Lu, Y. Liu, H. Lin, *et al.*, “Non-invasive imaging through dynamic scattering layers via speckle correlations,” *Opt. Rev.* **28**, 557–563 (2021).
21. L. E. Estes, L. M. Narducci, and R. A. Tuft, “Scattering of light from a rotating ground glass,” *J. Opt. Soc. Am.* **61**, 1301–1306 (1971).
22. V. S. Starovoitov, V. N. Chizhevsky, D. B. Horoshko, and S. Y. Kilin, “Spatio-temporal correlations of photons from a pseudo-thermal source,” *J. Appl. Spectrosc.* **90**, 377–387 (2023).
23. F. Trost, K. Ayyer, D. Oberthuer, *et al.*, “Speckle contrast of interfering fluorescence X-rays,” *J. Synchrotron Radiat.* **30**, 11–23 (2023).
24. C. Rosales-Guzmán and A. Forbes, *How to Shape Light with Spatial Light Modulators* (2017).
25. “Zenodo repository for data and codes,” [T.B.D.](https://zenodo.org/) (2024).
26. M. Bojer, J. Eckert, S. Karl, *et al.*, “Phase retrieval in incoherent diffractive imaging using higher-order photon correlation functions,” *New J. Phys.* **26**, 063014 (2024).
27. N. Peard, K. Ayyer, and H. N. Chapman, “Ab initio spatial phase retrieval via intensity triple correlations,” *Opt. Express* **31**, 25082–25092 (2023).
28. L. M. Lohse, M. Vassholz, and T. Salditt, “On incoherent diffractive imaging,” *Acta Crystallogr. Sect. A* **77**, 480–496 (2021).
29.  $I(\theta) \propto \cos^2\left(\frac{\pi d}{\lambda} \sin \theta\right) \times \sin^2\left(\frac{\pi r}{\lambda} \sin \theta\right)$ ,  $d \approx 1$  mm is the distance between the two Gaussian light sources,  $r \approx 100$   $\mu$ m is the root-mean-square size of each Gaussian light source and  $\theta$  is the observation angle.